

REPORTS

GEOMORPHOLOGY

Geophysical imaging reveals topographic stress control of bedrock weathering

J. St. Clair,^{1*} S. Moon,^{2*†} W. S. Holbrook,¹ J. T. Perron,² C. S. Riebe,¹ S. J. Martel,³ B. Carr,¹ C. Harman,⁴ K. Singha,⁵ D. deB. Richter⁶

Bedrock fracture systems facilitate weathering, allowing fresh mineral surfaces to interact with corrosive waters and biota from Earth's surface, while simultaneously promoting drainage of chemically equilibrated fluids. We show that topographic perturbations to regional stress fields explain bedrock fracture distributions, as revealed by seismic velocity and electrical resistivity surveys from three landscapes. The base of the fracture-rich zone mirrors surface topography where the ratio of horizontal compressive tectonic stresses to near-surface gravitational stresses is relatively large, and it parallels the surface topography where the ratio is relatively small. Three-dimensional stress calculations predict these results, suggesting that tectonic stresses interact with topography to influence bedrock disaggregation, groundwater flow, chemical weathering, and the depth of the "critical zone" in which many biogeochemical processes occur.

Weathered bedrock and soil are part of the life-sustaining layer at Earth's surface commonly referred to as the "critical zone." Its thickness depends on the competition between erosion, which removes weathered material from the land surface, and weathering, which breaks down rock mechanically and chemically and thus deepens the interface between weathered and fresh bedrock (1–3). Erosion at the surface can be studied both directly by observation (4) and indirectly using isotopic tracers (5). In contrast, weathering at depth is generally obscured by overlying rock and soil, making it more difficult to study. In this Report, we combine results from landscape-scale geophysical imaging and stress-field modeling to evaluate hypotheses about the relationship of subsurface weathering to surface topography.

One hypothesis is that weathering at depth is regulated by the hydraulic conductivity and porosity of bedrock and the incision rate of river channels into bedrock, which together determine

how rapidly groundwater flowing toward the river channels can drain bedrock pores of chemically equilibrated water (1). Another hypothesis, based on reactive transport modeling, predicts that the propagation of the weathered zone depends on the balance between mineral reaction kinetics and groundwater residence times (2, 6). These mechanisms are not mutually exclusive, and both emphasize the importance of fluid flow through bedrock. This implies that the development of fracture systems, which provide preferred fluid-flow paths in bedrock (7, 8), should help regulate the downward propagation of weathering.

Bedrock fractures may be inherited from past tectonic or thermal events, but the common observation that fracture abundance declines with depth (9) suggests that near-surface processes are capable of generating new fractures or reactivating existing ones. Examples of potential near-surface fracturing mechanisms include wedging due to growth of ice crystals (10), salt crystals (11), or roots (12); volume expansion due to weathering reactions of certain minerals (13); and stress perturbations associated with surface topography (14). Some of these mechanisms require specific conditions that only occur in certain geographic regions, rock types, or parts of the subsurface. For example, ice weathering requires repeated freeze-thaw cycles and is therefore limited to depths of a few meters, and volume expansion due to mineral weathering is most effective in rocks containing abundant biotite or hornblende. In contrast, surface topography always perturbs the bedrock stress field. Here we focus on this potentially widespread control on bedrock fractures.

Bedrock stress fields can be evaluated by considering the effects of local topography on grav-

itational stresses and regional tectonic stresses. Theoretical calculations have shown that the presence of topographic features such as ridges and valleys can cause vertical and lateral variations in the shallow subsurface stress field (15) and that these stress perturbations can be large enough to alter bedrock fracture patterns (14, 16). Some observational evidence suggests that topographic stresses influence near-surface fracture distributions (9, 17, 18) and groundwater flow (19–21), but it is unknown whether topographic stresses systematically affect the spatial distribution of bedrock weathering. In this study, we used geophysical surveys of seismic velocity and electrical resistivity to image the thickness of the weathered zone in three landscapes with similar topography but different tectonic stress conditions, and we tested whether the geometry of the weathered zone in each landscape matches the modeled topographic stress field.

A calculation of the stresses beneath an idealized topographic profile in the presence of regional tectonic stress illustrates how topographic stress might influence the geometry of the weathered zone (Fig. 1). We calculated the total stress field as the sum of the ambient stress due to gravity and tectonics and the stress perturbation due to topography (22). From the stress field, we calculated two scalar quantities that act as proxies for two mechanisms that could influence the abundance of fractures. As a proxy for shear fracturing or shear sliding on existing fractures, we calculated the failure potential (Φ) (23), defined as $(\sigma_{mc} - \sigma_{lc})/(\sigma_{mc} + \sigma_{lc})$, where σ indicates a stress, and the subscripts denote the most compressive (mc) and least compressive (lc) principal stresses, with compression being positive. As a proxy for opening-mode displacement on fractures, we used the magnitude of σ_{lc} . Because we do not have prior knowledge of the orientations or abundances of existing fractures in a given landscape, we used both quantities to represent the propensity for generating open fractures. A larger Φ indicates that new shear fractures are more likely to form and that existing fractures oriented obliquely to the σ_{mc} and σ_{lc} directions are more likely to dilate as a result of sliding on the rough fracture surfaces (24). A smaller σ_{lc} indicates that fractures oriented nearly perpendicular to the σ_{lc} direction will be more likely to open (20, 25). Given that open fractures permit water to flow more quickly through bedrock and enhance the rate of chemical weathering, we expect that zones of larger Φ or smaller σ_{lc} correspond to zones of more weathered bedrock.

In a scenario with a horizontal land surface and a stress field determined by both gravity and a low, uniform ambient horizontal compression, Φ declines and σ_{lc} increases with depth beneath the land surface (Fig. 1, A and D). If topography is added and the ambient horizontal compression remains low, contours of Φ and σ_{lc} generally parallel the surface (Fig. 1, B and E). This surface-parallel pattern occurs because σ_{lc} is determined primarily by the overburden in this scenario, and therefore it increases with

¹Department of Geology and Geophysics and Wyoming Center for Environmental Hydrology and Geophysics, University of Wyoming, Laramie, WY 82071, USA.

²Department of Earth, Atmospheric and Planetary Sciences, Massachusetts Institute of Technology, Cambridge, MA 02139, USA. ³Department of Geology and Geophysics, University of Hawaii, Honolulu, HI 96822, USA. ⁴Department of Geography and Environmental Engineering, The Johns Hopkins University, Baltimore, MD 21218, USA. ⁵Hydrologic Science and Engineering Program, Colorado School of Mines, Golden, CO 80401, USA. ⁶Nicholas School of the Environment, Duke University, Durham, NC 27708, USA.

*Corresponding author. E-mail: jstclair4@uwyo.edu (J.S.C.); sgmoon@mit.edu (S.M.) †These authors contributed equally to this work. ‡Present address: Department of Earth, Planetary, and Space Science, University of California–Los Angeles, Los Angeles, CA 90095, USA.

depth similarly beneath ridges and valleys (fig. S1A). However, if the ambient horizontal stress becomes strongly compressive—so that σ_{mc} at shallow depths parallels the topographic surface, and σ_{ic} becomes small relative to σ_{mc} (fig. S1, E and F)—then contours of Φ and σ_{ic} resemble mirror images of the land surface, plunging below ridges and rising beneath valleys (Fig. 1, C and F). This mirror-image pattern occurs because σ_{ic} becomes much smaller beneath ridges than beneath valleys, whereas the fractional decrease in σ_{mc} is relatively minor. In all three scenarios, spatial variations in σ_{ic} are the dominant cause of the spatial variations in Φ (Fig. 1, A to F, and fig. S1).

Where contours of Φ and σ_{ic} are generally parallel to the land surface, we expect to find a zone of abundant open fractures and weathered bedrock with a roughly uniform thickness, underlain by less weathered bedrock with fewer open fractures (Fig. 1, G and H). Where contours of Φ and σ_{ic} mirror the land surface, we expect to find thick weathered zones beneath ridges and thin zones beneath valleys (Fig. 1I). This conceptual model assumes that the geometry of the weathered zone reflects the present-day stress field. In an eroding landscape, a parcel of rock experiences a time-varying stress field as the eroding surface draws nearer. However, given that Φ increases and σ_{ic} decreases toward the surface (provided that the ambient horizontal tectonic stresses are compressive) (Fig. 1, A to F), the bottom boundary of the weathered zone is likely to be demarcated by the contour of the

lowest Φ or highest σ_{ic} at which fractures open enough to accelerate chemical weathering. After crossing this boundary, rocks will only experience higher Φ and lower σ_{ic} and should become even more weathered.

A dimensionless ratio of tectonic stresses to gravitational stresses that accounts for topographic perturbations captures the difference between the surface-parallel scenario (Fig. 1, B, E, and H) and the surface-mirroring scenario (Fig. 1, C, F, and I). This ratio is defined as

$$\sigma^* = \frac{\sigma_t b/a}{\rho g b} = \frac{\sigma_t}{\rho g a} \quad (1)$$

where σ_t is the magnitude of the horizontal tectonic stress perpendicular to the ridges and valleys, which we refer to as the tectonic compression; b/a is the characteristic slope of a topographic feature with height b and horizontal length a ; ρ is rock density; and g is gravitational acceleration. Our model predicts that a landscape with $\sigma^* < -1$, corresponding to low tectonic compression or widely spaced ridges and valleys, should have a zone of large Φ , small σ_{ic} , and weathered rock that parallels the surface topography (Fig. 1, B, E, and H). Conversely, a landscape with $\sigma^* > -1$, corresponding to high tectonic compression or closely spaced ridges and valleys, should have a zone of large Φ , small σ_{ic} , and weathered rock that thickens under ridges and thins under valleys (Fig. 1, C, F, and I). The surface-mirroring pattern is most pronounced for landscapes with $b/a > 0.05$.

To test our conceptual model, we investigated three field sites in the United States with similar topography but different ambient tectonic stress regimes. Gordon Gulch (Fig. 2B), in the Boulder Creek Critical Zone Observatory, Colorado (3), is underlain by Precambrian gneiss and has weak tectonic compression ($\sigma_t = 1$ MPa; $\sigma^* = 0.2$). Calhoun Critical Zone Observatory, South Carolina (Fig. 2C) (26), is underlain by Neoproterozoic or Cambrian granite gneiss and has stronger tectonic compression ($\sigma_t = 4.7$ MPa; $\sigma^* = 1.2$). Pond Branch, Maryland (Fig. 2D) (27), is underlain by Precambrian schist and has the strongest tectonic compression of the three sites ($\sigma_t = 8.4$ MPa; $\sigma^* = 3.2$). At each site, we selected a valley with a cross-sectional relief of 20 to 40 m and used a three-dimensional stress model to calculate the topographic perturbation to the ambient stress field in the vicinity of the valley (22). Our model calculations include ~ 1 to 15 km² of the topography surrounding our field sites (Fig. 2). Ambient stress magnitudes, directions, and depth gradients were constrained from compilations of regional measurements (fig. S2) (22).

Transects of Φ and σ_{ic} across the valleys (Fig. 3, A to F) show patterns consistent with the idealized calculations shown in Fig. 1, A to F. A zone of high Φ and low σ_{ic} , with roughly uniform depth, parallels the land surface at Gordon Gulch ($\sigma^* = 0.2$) (Fig. 3, A and D), whereas the zones of high Φ and low σ_{ic} at Calhoun ($\sigma^* = 1.2$) and Pond Branch ($\sigma^* = 3.2$) are deeper beneath ridges and shallower beneath valleys (Fig. 3, B, C, E, and F). Sensitivity tests accounting for uncertainties in

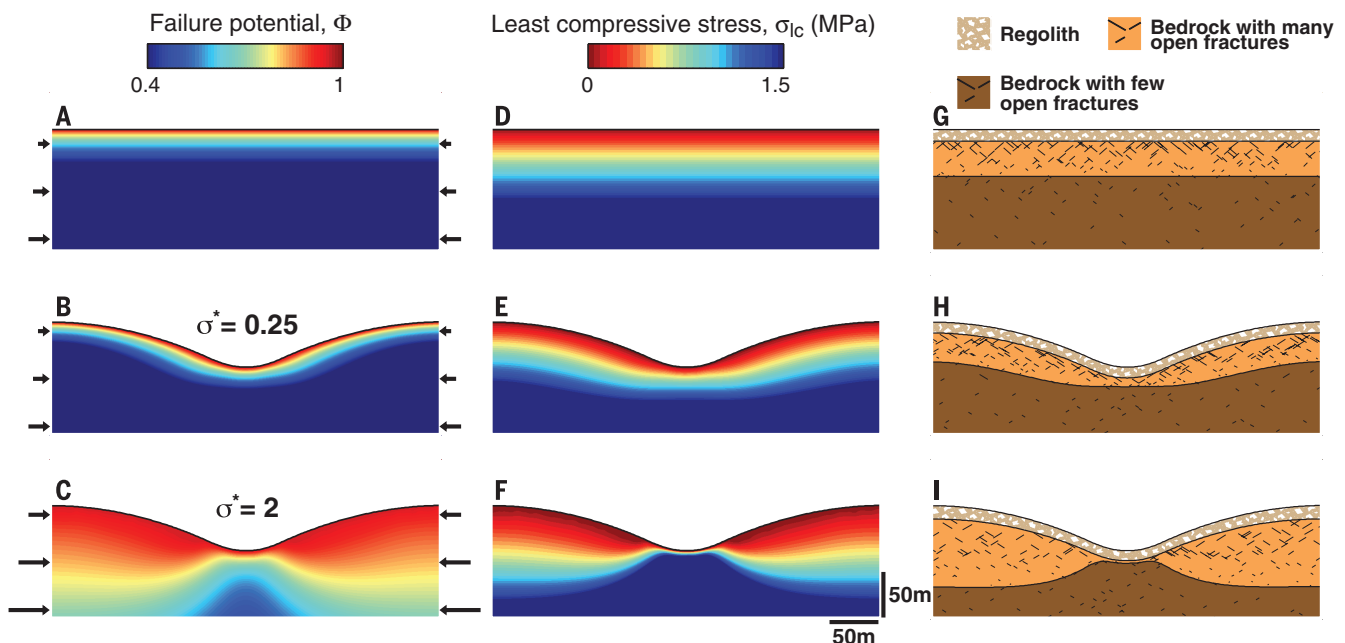


Fig. 1. Hypothesized influence of topography and tectonic stress on weathering zone geometry. (A to C) Cross-sectional plots of failure potential (Φ) computed with a numerical stress model (22). Arrows indicate the magnitude of ambient horizontal compression. (A) shows a horizontal surface under weak compression, (B) shows ridges and valleys under weak compression, and (C) shows ridges and valleys under strong compression. The magnitude of the horizontal compression at the mean elevation of the land

surface is $0.25\rho ga$ in (A) and (B) and $2\rho ga$ in (C), where ρ is rock density, g is gravitational acceleration, and a is the horizontal distance from the valley bottom to the ridge top in (B) and (C). This corresponds to σ^* values of 0.25 in (B) and 2 in (C) (Eq. 1). Topography is horizontally periodic. (D to F) The same scenarios as in (A) to (C), but showing the magnitude of the least compressive principal stress, σ_{ic} . (G to I) Conceptual diagrams of bedrock fracture abundance in the three scenarios.

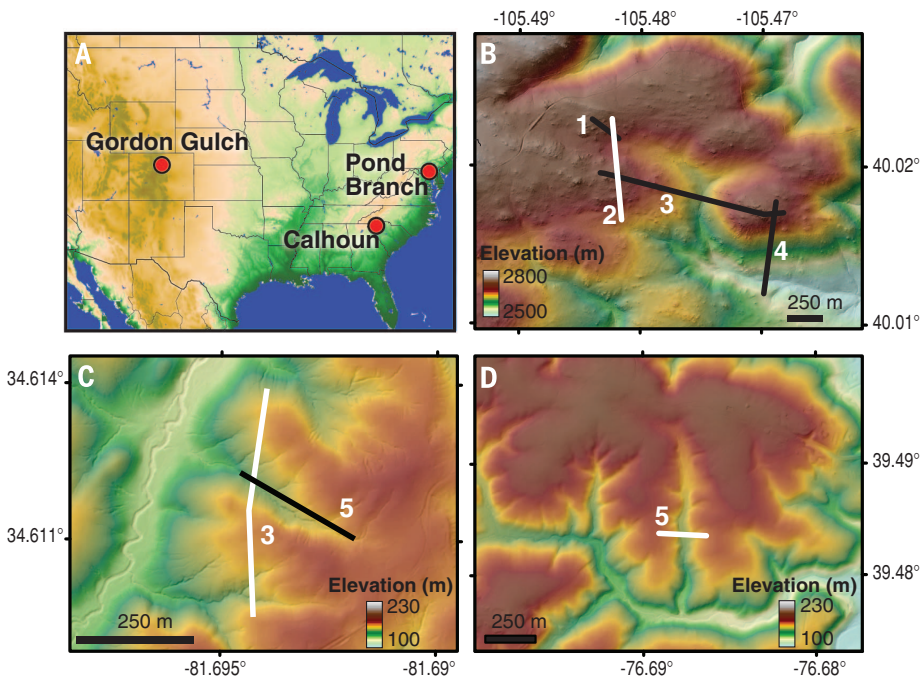


Fig. 2. Maps of study sites. (A) Locations of the three U.S. sites. Colors indicate elevation, with greens being lowest and browns being highest. (B) Gordon Gulch, Colorado. (C) Calhoun, South Carolina. (D) Pond Branch, Maryland. Geophysical survey lines are numbered. White lines mark the transects shown in Fig. 3. Elevation data are from the U.S. National Elevation Dataset and the National Center for Airborne Laser Mapping.

the ambient stress estimates and variations in topography across the sites confirm that these patterns are robust (fig. S3 to S5) (22).

We performed seismic refraction and electrical resistivity surveys along the same transects to investigate whether topographic stresses influence the geometry of the weathered zone (22). The seismic velocity structure reflects variations in rock damage such as chemical weathering and fracturing (28), both of which contribute to an increase in porosity and a decrease in seismic velocity (29). Velocity in fractured rocks can also increase with higher water saturation, which increases the effective bulk modulus of the composite medium (28, 30), or higher confining stress, which closes microfractures formed during the rock's thermal and tectonic history (31). We observed steep velocity gradients with depth, with P -wave velocities (v_p) increasing downward from ~ 0.3 km/s near the surface to ~ 4.0 to 4.5 km/s at 10 to 40 m depth (Fig. 3, G to I), consistent with a transition from soil regolith to unweathered bedrock (28). The rapid increase in velocity with depth is likely also due in part to closure of fractures with increasing confining stress (31). At depths greater than the 4-km/s velocity contour, fractures are likely to be effectively closed, and the velocity gradients are greatly reduced. Borehole observations, including velocity measurements at fine depth increments (fig. S7B) and fractures mapped in optical image logs (fig. S10)

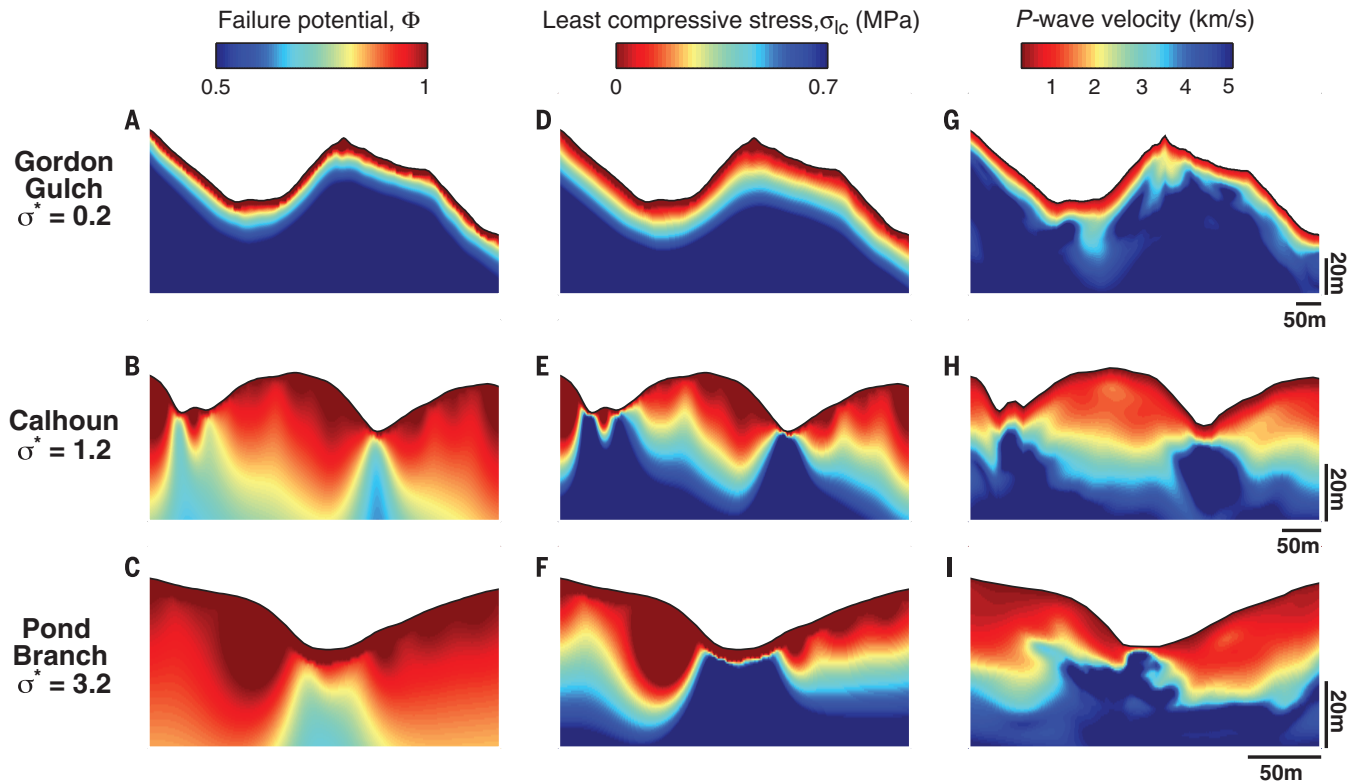


Fig. 3. Comparisons of topographic stress and seismic velocity. Modeled failure potential (A to C), modeled magnitude of the least compressive stress (D to F), and measured P -wave velocity (G to I) for Gordon Gulch [(A), (D), and (G)], Calhoun [(B), (E), and (H)], and Pond Branch [(C), (F), and (I)]. Transect locations are marked in white in Fig. 2. The topographic surface was smoothed for stress calculations (17). Vertical exaggerations are 3.6 \times at Gordon Gulch, 3.7 \times at Calhoun, and 2.3 \times at Pond Branch.

(22), support the interpretation that faster velocities correspond to less abundant open fractures.

The variations in seismic velocity are highly similar in shape to the variations in modeled Φ and σ_{1c} , particularly in the zones of low velocity ($v_p < 4$ km/s; Fig. 3, G to I), which generally correspond to zones of high Φ ($\Phi > 0.75$; Fig. 3, A to C) and low σ_{1c} ($\sigma_{1c} < 0.5$ MPa; Fig. 3, D to F). The 4-km/s velocity contour rises to within 10 m of the surface beneath valley bottoms and plunges to depths of 40 m beneath ridgetops at the sites with strong tectonic compression and $\sigma^* > 1$ (Fig. 3, H and I). This is very similar to the mirror-image pattern of Φ and σ_{1c} contours that is predicted by the stress model (Fig. 3, B, C, E, and F). In contrast to these sites, both the 4-km/s velocity contour and the zones of high Φ and low σ_{1c} roughly parallel the land surface at Gordon Gulch (Fig. 3, A, D, and G), which has weak tectonic compression and $\sigma^* < 1$. The velocity fields contain some fine-scale structures that do not appear in the modeled stress fields, but the stress models do predict some secondary features of the velocity structure. For example, the zones of high Φ and low seismic velocity at Pond Branch are both thicker beneath the right-hand side of the valley bottom (Fig. 3, C and F), and the zone of low σ_{1c} shows this asymmetry for slightly smaller values of σ^* (fig. S4D). The bases of these three zones slope down to the right beneath both ridges at Calhoun (Fig. 3, B, E, and H).

At all three sites, Φ and σ_{1c} correlate well with seismic velocity (fig. S8). The trends of σ_{1c} versus v_p for the three sites are very similar (fig. S8, D to F), whereas the trends of Φ versus v_p (fig. S8, A to C), particularly at Gordon Gulch. This may indicate that opening of fractures oriented perpendicular to the σ_{1c} direction is a stronger control on seismic velocity than shear fracturing or sliding at these sites, or it may reflect differences in rock properties among sites that influence the relationship between stress and seismic velocity. In general, the strong correspondence between Φ , σ_{1c} , and seismic velocity at these sites suggests a robust influence of topographic stress on the physical state of weathered bedrock in the subsurface.

We measured electrical resistivity to determine whether the zones of high Φ , low σ_{1c} , and low seismic velocity also have high water

content and more weathered rock. Rocks become less electrically resistive with increasing water saturation, connectedness of pores, and clay content (32). The resistivity images show structures similar to those in the seismic velocity images and reveal additional details about the hydrology of the weathered zone. For example, resistivity at Calhoun increases with depth, and we identified three regions that roughly correlate with the seismic velocity structure (Fig. 4). Where seismic velocities exceed 4 km/s, resistivity is generally high (>4000 ohm-m), consistent with low water content and poorly connected pores in intact bedrock. The upper 10 m of the weathered zone has low resistivity (100 to 700 ohm-m) and velocities < 1.5 km/s, consistent with a highly porous, water-saturated regolith. Between these zones is a zone of intermediate resistivity (700 to 4000 ohm-m) and velocity (1.5 to 4.0 km/s), consistent with fractured, slightly weathered bedrock with intermediate water content. We additionally observed a resistive body roughly 10 m beneath the ridgetop that has higher seismic velocity than the surrounding rock and is in close proximity to a region of locally reduced Φ and elevated σ_{1c} (Fig. 3, B and E).

The geophysical observations support the hypothesis that topographic stress influences bedrock weathering by modifying the abundance of open fractures. This interpretation is consistent with the borehole sonic velocity log at Calhoun (fig. S7B) and the borehole image logs at Gordon Gulch (fig. S10) (22), both of which show lower velocities where fractures are more abundant. However, it is important to consider how factors other than fracture abundance might influence seismic velocity and resistivity. Higher water saturation can elevate seismic velocity, but our resistivity maps show the opposite: a near-surface layer with high water content but lower velocity (Fig. 4). Stress-induced pore pressure variations are also an unlikely explanation for the observed seismic velocity variations, because the velocity field resembles the least compressive stress rather than the mean stress. A more likely scenario is that areas with lower velocities and lower resistivity have experienced a higher degree of chemical weathering. This possibility does not conflict with the interpretation that fractures influence

velocity and resistivity variations; more abundant, open, and connected fractures should promote faster groundwater flow and chemical weathering, which would enhance the connection between topographic stress and bedrock damage.

Our results suggest that topographic perturbations to gravitational and tectonic stress fields control the distribution of open fractures, permeability, and water storage potential in a weathered subsurface zone with a thickness comparable to the topographic relief. We propose that the base of the weathered zone is the depth above which stresses allow abundant fractures to grow or open, providing pathways for water and biota to invade the bedrock and initiate weathering. The stress field thus sets the physical stage for the interacting geochemical (2), hydrological (1), biological (33), and climatic (3) processes that drive weathering and nutrient cycling in Earth's critical zone, which in turn help regulate the global carbon cycle (6). Lateral variations in stress-mediated weathering may also lead to variations in bedrock erodibility and the production rate of mobile soil. Topographic stress may ultimately govern the evolution of landforms through its influence on subsurface weathering and, thus, on erosion at the surface.

REFERENCES AND NOTES

1. D. M. Rempe, W. E. Dietrich, *Proc. Natl. Acad. Sci. U.S.A.* **111**, 6576–6581 (2014).
2. M. I. Lebedeva, S. L. Brantley, *Earth Surf. Process. Landf.* **38**, 1793–1807 (2013).
3. R. S. Anderson, S. P. Anderson, G. E. Tucker, *Earth Surf. Process. Landf.* **38**, 299–316 (2013).
4. J. D. Milliman, K. L. Farnsworth, *River Discharge to the Coastal Ocean: A Global Synthesis* (Cambridge Univ. Press, New York, 2011).
5. J. L. Dixon, C. S. Riebe, *Elements* **10**, 363–368 (2014).
6. K. Maher, C. P. Chamberlain, *Science* **343**, 1502–1504 (2014).
7. J. C. S. Long *et al.*, *Int. J. Rock Mech. Min. Sci.* **28**, 121–142 (1991).
8. R. Owen, A. Maziti, T. Dahlin, *Hydrogeol. J.* **15**, 1231–1238 (2007).
9. M. Slim, J. Perron, S. J. Martel, K. Singha, *Earth Surf. Process. Landf.* **40**, 512–529 (2015).
10. J. S. Walder, B. Hallet, *Arct. Alp. Res.* **18**, 27–32 (1986).
11. H. W. Wellman, A. T. Wilson, *Nature* **205**, 1097–1098 (1965).
12. J. J. Roering, J. Marshall, A. M. Booth, M. Mort, Q. Jin, *Earth Planet. Sci. Lett.* **298**, 183–190 (2010).
13. H. L. Buss, P. B. Sak, S. M. Webb, S. L. Brantley, *Geochim. Cosmochim. Acta* **72**, 4488–4507 (2008).
14. D. J. Miller, T. Dunne, *J. Geophys. Res.* **101**, 25,523–25,536 (1996).
15. W. Z. Savage, H. S. Swolfs, *J. Geophys. Res.* **91**, 3677–3685 (1986).
16. P. Molnar, *J. Geophys. Res.* **109**, F02010 (2004).
17. S. J. Martel, *Geophys. Res. Lett.* **33**, L01308 (2006).
18. S. J. Martel, *Geophys. Res. Lett.* **30**, L20303 (2011).
19. P. Upton, R. Sutherland, *Earth Planet. Sci. Lett.* **389**, 176–187 (2014).
20. C. A. Barton, D. Moos, M. D. Zoback, *Leading Edge* **16**, 1653–1656 (1997).
21. R. H. Morin, W. Z. Savage, *J. Geophys. Res.* **107**, 2340 (2002).
22. Materials and methods are available as supplementary materials on Science Online.
23. R. M. Iverson, M. E. Reid, *Water Resour. Res.* **28**, 925–938 (1992).
24. I. W. Yeo, R. W. De Freitas, R. W. Zimmerman, *Int. J. Rock Mech. Min. Sci.* **35**, 1051–1070 (1998).

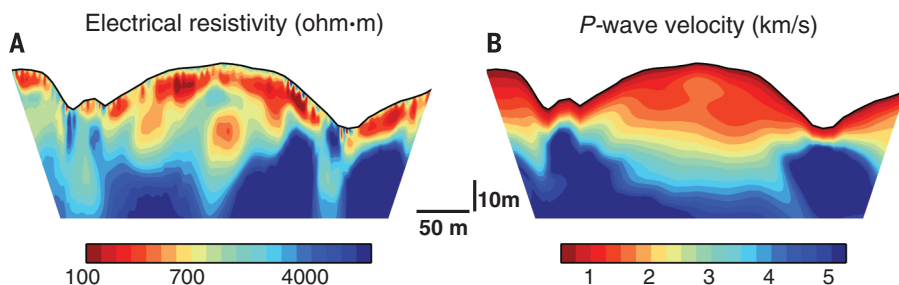


Fig. 4. Electrical resistivity and seismic velocity at the Calhoun site. The transect is the same as in Fig. 3, B, E, and H. Resistivity (A) and P -wave velocity (B) increase with depth, probably reflecting the closing of fractures. Both images show the surface-mirroring pattern predicted by the stress model (Fig. 3, B and E). Vertical exaggeration is 3 \times .

25. K. B. Min, J. Rutqvist, C. F. Tsang, L. Jing, *Int. J. Rock Mech. Min. Sci.* **41**, 1191–1210 (2004).
26. D. Richter, S. A. Billings, *New Phytol.* **206**, 900–912 (2015).
27. E. T. Cleaves, A. E. Godfrey, O. P. Bricker, *Geol. Soc. Am. Bull.* **81**, 3015–3032 (1970).
28. N. Barton, *Rock Quality, Seismic Velocity, Attenuation and Anisotropy* (Taylor and Francis Group, London, 2006).
29. W. S. Holbrook et al., *Earth Surf. Process. Landf.* **39**, 366–380 (2014).
30. A. Nur, G. Simmons, *Earth Planet. Sci. Lett.* **7**, 183–193 (1969).
31. O. O. Blake, D. R. Faulkner, A. Rietbrock, *Pure Appl. Geophys.* **170**, 493–505 (2013).
32. G. E. Archie, *Trans. Am. Inst. Min. Metall. Pet. Eng.* **146**, 54–62 (1942).
33. D. W. Schwartzman, T. Volk, *Nature* **340**, 457–460 (1989).

ACKNOWLEDGMENTS

This study was supported by the NSF Experimental Program to Stimulate Competitive Research (award EPS-1208909), the U.S. Army Research Office (grant W911NF-14-1-0037), NSF Earth Sciences (awards EAR-0724960 to the University of Colorado–Boulder and EAR-1331846 to Duke University), and the NSF Critical Zone Observatory Network. Poly3D software was provided by Schlumberger. 3DMove software was provided by Midland Valley Software. Geophysical data presented in this paper

are available through the Wyoming Center for Environmental Hydrology and Geophysics data repository at http://ecoinfo.wyisc.org/data-archive#PB_CCZO_BCCZO. The authors thank the editor and three anonymous reviewers for their suggestions.

SUPPLEMENTARY MATERIALS

www.sciencemag.org/content/350/6260/534/suppl/DC1
Materials and Methods
Figs. S1 to S10
Tables S1 to S3
References (34–55)

27 March 2015; accepted 25 August 2015
10.1126/science.aab2210

MAGNETISM

Mobile metallic domain walls in an all-in-all-out magnetic insulator

Eric Yue Ma,^{1,2*} Yong-Tao Cui,^{1*} Kentaro Ueda,^{3,4*} Shujie Tang,^{1,5} Kai Chen,⁶ Nobumichi Tamura,⁷ Phillip M. Wu,¹ Jun Fujioka,^{3,4} Yoshinori Tokura,^{3,4†} Zhi-Xun Shen^{1,2†}

Magnetic domain walls are boundaries between regions with different configurations of the same magnetic order. In a magnetic insulator, where the magnetic order is tied to its bulk insulating property, it has been postulated that electrical properties are drastically different along the domain walls, where the order is inevitably disturbed. Here we report the discovery of highly conductive magnetic domain walls in a magnetic insulator, $\text{Nd}_2\text{Ir}_2\text{O}_7$, that has an unusual all-in-all-out magnetic order, via transport and spatially resolved microwave impedance microscopy. The domain walls have a virtually temperature-independent sheet resistance of ~ 1 kilohm per square, show smooth morphology with no preferred orientation, are free from pinning by disorders, and have strong thermal and magnetic field responses that agree with expectations for all-in-all-out magnetic order.

Magnetic order, in particular antiferromagnetism, often accompanies metal-insulator transitions (MITs), during which metallic materials abruptly become insulating or semiconducting at certain critical temperatures (*T*). Whether metallic behavior can be recovered in these magnetic insulators at magnetic domain walls (DWs), where the order is inevitably disturbed, is a long-standing question that is widely addressed theoretically but remains elusive experimentally (2–5). A related but distinct situation is that of conductive ferroelectric DWs in ferroelectric insulators, the discovery of which has opened a broad field of

research dedicated to understanding the fundamental mechanism, as well as making practical DW-based devices (6–9). However, among the vast array of magnetic insulators, no conductive magnetic DW has been firmly identified so far. Recently, bulk measurements have provided signatures of DW conduction in the low-temperature insulating phase of $\text{Nd}_2\text{Ir}_2\text{O}_7$ (10), a candidate for the exotic “Weyl semimetal” with an unusual all-in-all-out magnetic order (11–16). Here we combine bulk measurements with local-conductivity-measuring microwave impedance microscopy (MIM) to directly resolve highly conductive DWs in $\text{Nd}_2\text{Ir}_2\text{O}_7$ in real space. These results rule out alternative contributions and thus provide evidence for a realization of conduction due to the discontinuity of magnetic order.

$\text{Nd}_2\text{Ir}_2\text{O}_7$ is a pyrochlore iridate in which the electronic states near Fermi energy are dominated by t_{2g} electrons from Ir atoms (17). It undergoes a MIT at a Néel temperature $T_N \sim 32$ K (Fig. 1A), with a concomitant all-in-all-out (AIAO) magnetic order developing for the Ir magnetic moments (14, 18, 19): The Ir moments at the four vertices of each corner-sharing tetrahedron all point either inward or outward in an alternating manner (Fig. 1B). This unusual magnetic order is a ferroic order of magnetic octupole and preserves the symmetry of the underlying lattice (13). For a

given lattice, there are two and only two distinct variations of the order: all-in-all-out (AIAO) and all-out-all-in (AOAI). They represent opposite magnetic octupoles and are interchanged with each other by time-reversal transformation; by contrast, their electronic properties should be identical in the absence of external perturbations.

Nonetheless, abnormal conduction can happen at the boundaries between AIAO and AOAI domains (i.e., magnetic DWs), as hinted by macroscopic transport measurements (10): The resistance of the same polycrystalline sample at 4.5 K after cooling from above T_N in zero field (ZFC or “untrained”) can be more than a factor of 200 smaller than that cooled in a 9-T field (FC or “trained”) (Fig. 1A). One may attribute the extra conduction to DWs, with field cooling resulting in fewer magnetic domains, fewer DWs, and thus higher overall resistance. However, alternative explanations, including history dependence of the bulk and grain boundaries, cannot be ruled out by these macroscopic measurements.

We confirm the existence of highly conductive magnetic DWs by direct imaging with MIM, a scanning probe technique that senses local conductivity by measuring tip-sample impedance at ~ 1 GHz (20–22): More conductive regions screen the microwave electric field better, resulting in a smaller tip-sample impedance. Working at high frequency eliminates the need of a back electrode and a complete current path, making MIM ideal for bulk insulating samples (23). Figure 1C is an $18 \mu\text{m}$ by $18 \mu\text{m}$ MIM scan of a polished $\text{Nd}_2\text{Ir}_2\text{O}_7$ polycrystal surface (fig. S1A) at 4.7 K after cooling in zero field (untrained). Smooth curvilinear features that are much more conductive than the bulk exist in all grains, with an apparent width of ~ 100 nm, similar to the spatial resolution of MIM in this particular experiment (fig. S2). They are continuous within individual grains, show no preferred orientations, and either form closed loops or terminate at the grain boundaries, but they never form vertices. As a result, each grain is divided into regions that can be assigned using only two labels, as expected for AIAO order, which has only two variations. Interestingly, many DWs from adjacent grains are in close proximity at the grain boundaries (yellow arrows in Fig. 1C). Such proximity may facilitate transport across grain boundaries and enhance the DW contribution to the measured conductance in macroscopic polycrystalline samples (10). We stress here that the

¹Geballe Laboratory for Advanced Materials (GLAM), Stanford University, Stanford, CA, USA. ²Department of Applied Physics, Stanford University, Stanford, CA, USA. ³Department of Applied Physics, University of Tokyo, Tokyo, Japan. ⁴RIKEN Center for Emergent Matter Science (CEMS), Saitama, Japan. ⁵State Key Laboratory of Functional Materials for Informatics, Shanghai Institute of Microsystem and Information Technology (SIMIT), Shanghai, China. ⁶Center for Advancing Materials Performance from the Nanoscale (CAMP-Nano), State Key Laboratory for Mechanical Behavior of Materials, Xi'an Jiaotong University, Xi'an, China. ⁷Advanced Light Source (ALS), Lawrence Berkeley National Laboratory, Berkeley, CA, USA.
*These authors contributed equally to this work. †Corresponding author. E-mail: tokura@riken.jp (Y.T.); zxshen@stanford.edu (Z.-X.S.)

This copy is for your personal, non-commercial use only.

If you wish to distribute this article to others, you can order high-quality copies for your colleagues, clients, or customers by [clicking here](#).

Permission to republish or repurpose articles or portions of articles can be obtained by following the guidelines [here](#).

The following resources related to this article are available online at www.sciencemag.org (this information is current as of October 30, 2015):

Updated information and services, including high-resolution figures, can be found in the online version of this article at:

<http://www.sciencemag.org/content/350/6260/534.full.html>

Supporting Online Material can be found at:

<http://www.sciencemag.org/content/suppl/2015/10/28/350.6260.534.DC1.html>

A list of selected additional articles on the Science Web sites **related to this article** can be found at:

<http://www.sciencemag.org/content/350/6260/534.full.html#related>

This article **cites 40 articles**, 6 of which can be accessed free:

<http://www.sciencemag.org/content/350/6260/534.full.html#ref-list-1>

This article has been **cited by** 1 articles hosted by HighWire Press; see:

<http://www.sciencemag.org/content/350/6260/534.full.html#related-urls>